Journal of Power Sources 383 (2018) 102–109

Contents lists available at ScienceDirect

Journal of Power Sources

journal homepage: www.elsevier.com/locate/jpowsour

High-energy green supercapacitor driven by ionic liquid electrolytes as an ultra-high stable next-generation energy storage device

Ranjith Thangavel[a], Aravindaraj G. Kannan[b], Rubha Ponraj[b], Vigneysh Thangavel[c], Dong-Won Kim[b], Yun-Sung Lee[a,*]

[a] Faculty of Applied Chemical Engineering, Chonnam National University, Gwang-ju 500-757, Republic of Korea
[b] Department of Chemical Engineering, Hanyang University, Seoul 04763, Republic of Korea
[c] Department of Electrical and Electronics Engineering, Institute of Aeronautical Engineering, Hyderabad 500 043, Telangana, India

HIGHLIGHTS

- Hierarchal porous carbon is obtained from waste watermelon rind.
- The biomass carbon exhibits high surface area along with micro and mesopores.
- A high voltage supercapacitor is constructed with ionic liquid electrolyte.
- The supercapacitor delivers high energy (174 Wh kg^{-1}) and high power (20 kW kg^{-1}).
- The supercapacitor exhibits remarkable stability (150,000 cycles) at 60 °C.

ARTICLE INFO

Keywords:
Supercapacitor
Bio-mass
Ionic liquid
Energy storage
Electrolyte

ABSTRACT

Development of supercapacitors with high energy density and long cycle life using sustainable materials for next-generation applications is of paramount importance. The ongoing challenge is to elevate the energy density of supercapacitors on par with batteries, while upholding the power and cyclability. In addition, attaining such superior performance with green and sustainable bio-mass derived compounds is very crucial to address the rising environmental concerns. Herein, we demonstrate the use of watermelon rind, a bio-waste from watermelons, towards high energy, and ultra-stable high temperature green supercapacitors with a high-voltage ionic liquid electrolyte. Supercapacitors assembled with ultra-high surface area, hierarchically porous carbon exhibits a remarkable performance both at room temperature and at high temperature (60 °C) with maximum energy densities of ~174 Wh kg^{-1} (25 °C), and 177 Wh kg^{-1} (60 °C) – based on active mass of both electrodes. Furthermore, an ultra-high specific power of ~20 kW kg^{-1} along with an ultra-stable cycling performance with 90% retention over 150,000 cycles has been achieved even at 60 °C, outperforming supercapacitors assembled with other carbon based materials. These results demonstrate the potential to develop high-performing, green energy storage devices using eco-friendly materials for next generation electric vehicles and other advanced energy storage systems.

1. Introduction

The ever increasing global energy demand, the reduced availability of fossil fuels and rising environmental concerns have shifted the focus of energy research toward the development of sustainable and renewable energy sources such as solar and wind energy [1,2]. However, these energy sources are highly intermittent in nature and require grid-scale energy storage devices for back-up and load-leveling during peak production and consumption periods, respectively. Moreover, the energy-intensive automotive sector requires electric vehicles with low CO_2 emissions. To meet the demands of these next-generation applications, a significant improvement in the energy density and cycle life of current energy storage devices is crucial [3]. However, the current state-of-the-art lithium ion batteries have almost reached their practical limit [4,5]. Although sodium ion batteries are being developed due to their low cost, their energy density is lower than that achievable in lithium ion batteries. Specifically, problems related to low specific power and poor cycle life limit the practical use of these battery systems [6,7]. On the other hand, supercapacitors are highly promising candidates for next-generation applications due to their high power densities

* Corresponding author.
E-mail address: leeys@chonnam.ac.kr (Y.-S. Lee).

https://doi.org/10.1016/j.jpowsour.2018.02.037
Received 23 November 2017; Received in revised form 29 January 2018; Accepted 14 February 2018
Available online 24 February 2018
0378-7753/

and long cycle life [8,9].

Supercapacitors have been receiving increased interest due to their high power density and long cycle life. They can work as an independent energy source or complement different energy sources such as batteries, fuel cells, solar cells and wind power, where quick bursts of power are required [3,10]. Supercapacitors are generally classified as non-faradic electrical double layer type charge accumulation at the porous carbon electrode-electrolyte interface, and pseudocapacitors based on reversible faradaic redox surface charge storage in metal oxides/sulfides [9,11–14].

Supercapacitors based on double layer formation are always an eminent choice for commercial devices due to their simple construction and long cycle life than pseudocapacitors. Porous carbon-based materials have been widely used in double layer type supercapacitors due to their high surface area, which provides large number of favorable sites for double layer formation [15,16]. Recently, supercapacitors exhibiting high energy densities closer to those of rechargeable batteries and power densities much higher than those of batteries have been reported [17,18]. Moreover, the energy density of supercapacitors can be further increased by extending the operating potential using ionic liquid electrolytes and high surface area carbon architecture [19–21]. However, supercapacitors employing ionic liquid electrolytes suffer from relatively poor cycling performance and failure at high power due to the highly viscous nature of the ionic liquid. This can be overcome by employing a high surface area carbon with mesoporous hierarchical architecture and favorable functional groups that could aid penetration of ionic liquids into deeper pores and get stored for a longer time [20,22].

Activated carbons, the widely used candidate of choice for double layer type supercapacitors deliver unsatisfactory performance with highly viscous and low diffusivity ionic liquids [23,24]. The highly micrporous conventional activated carbon cannot provide space for large sized ions in ionic liquids, curtailing the performance of supercapacitor device [25–27]. Various forms of carbon with wider pores have been extensively explored including graphene, carbon nanofibers, carbon nanotubes, template-derived carbon and porous carbon [28–32]. Although graphene and template-derived carbons are considered to be more promising, there are major challenges that impede the practical application of these materials including graphene restacking during processing, poor control over pore distribution and the tedious process required for template preparation [33,34].

Bio-mass, which is widely an agricultural waste has recently emerged as an alternate source for porous carbon and has been adapted in energy storage devices [35,36]. Bio-mass derived porous carbon can achieve ultra-high surface area than graphene, along with tailored architecture, large pore volume, mesoporous morphology, tuned surface chemistry and wide commercial viability [37,38]. In addition, porous carbon produced from bio-wastes can provide a sustainable solution due to its renewable nature, low cost and wide availability [32,39]. The major research involves investigation of bio-mass derived porous carbon towards low energy aqueous supercapacitors, lacking exploration in high performing - high energy supercapacitors.

Herein, we report the application of highly mesoporous carbon derived from waste watermelon rind (hereafter referred as CWM) with a hierarchical pore structure and controlled pore morphology towards high energy supercapacitors driven by high voltage ionic liquid electrolyte. Watermelon rind is a bio-waste that constitutes about 33% of watermelon material (*Citrullus lanatus*). The worldwide production of watermelons is more than 100 million tons per year and waste watermelon rind are an inexpensive, and abundantly available carbon precursor that could enable the possibility of sustainable and green high energy – high power next generation devices. Although, porous carbon from watermelon peels have been investigated for supercapacitor applications, the most of the research focuses on capacitor working with aqueous electrolytes with a limited working potential [29,36–38]. Additionally, the true and practical merits with symmetrical two electrode testing has not been widely investigated. In this research, we evaluate the performance of such symmetrical supercapacitor working in an ionic liquid electrolyte under a wide working potential (4V) and at elevated temperature. The current research establishes the possibilities of utilizing sustainable, high energy storage systems for advanced applications.

2. Experimental

2.1. Synthesis of CWMs

Watermelons used in this work were purchased from local markets in Korea, and the rind was collected after removing the edible portions. The rind was rinsed with DI water and dried in an oven at 120 °C, and it was then powdered prior to the carbonization step. Carbonization was carried out at 600 °C in an Ar atmosphere. Chemical activation with KOH was used to generate pores, and the ratio of carbon to KOH was controlled to be 1:5. After activation in a tube furnace at 800 °C for 2 h in an Ar atmosphere, the product was washed with a 0.1 M HCl solution, followed by rinsing with water and ethanol several times. The material was then dried and used for further characterization and supercapacitor performance evaluation.

2.2. Material characterization

The morphologies of the CWM were characterized using scanning electron microscopy (SEM, JEOL JSM 6701F) equipped with energy dispersive spectroscopy (EDS) and high-resolution transmission electron microscopy (HRTEM, JEOL, JEM 2100F). X-ray diffraction (XRD, Rigaku D/MAX 2500 diffractometer) was used to characterize the crystalline structure of CWM. X-ray photoelectron spectroscopy (XPS, VG Multilab ESCA System, 220i) was used to confirm carbonization and to characterize the surface functional groups. Nitrogen adsorption/desorption isotherms were recorded using an ASAP-2020, Micromeritics, USA apparatus at 77 K. The powder samples were degassed at 300 °C for 2 h under vacuum prior to the measurements. The micropore size distribution were determined based on non-local density functional theory (NLDFT) assuming a slit pore model. The mesopore distribution was determined based on Barrett-Joyner-Halenda (BJH) model. Raman spectra were obtained using a Dongwoo Optron, MonoRa 780i spectrometer. The electrical conductivity of the carbon powders were determined in four pin probe apparatus (Loresta-GP MCP-T610, Mitsubishi chemical analytech) at 25 °C using a carbon pellet (1 cm diameter) pressed at 10 MPa. The contact angle measurement of the electrodes with ionic liquid electrolyte was measured on Kruss DSA100 Goniometer.

2.3. Electrochemical characterization

The electrodes for supercapacitor were formulated with accurately weighed amounts of active material (80 wt%), Ketjen black (10 wt%) as conductive carbon, and Teflonized acetylene black binder (10 wt%). The electrode was pressed over a stainless-steel mesh with a mass loading of 2.5–3.5 mg cm^{-2} and dried at 160 °C for 4 h in a vacuum oven. The thickness of the working electrode is calculated to be ~70-75 μm. Supercapacitors were assembled in a standard CR2032 coin cell with two symmetrical electrodes, which were separated by a porous polypropylene separator (Celgard 3401) and filled with 1-ethyl-3-methylimidazolium bis(trifluoromethylsulfonyl)imide (EMImTFSI). EMImTFSI was purchased from Chem Tech Research Incorporation and was used after drying under vacuum at 100 °C for 24 h. The water content in EMImTFSI after drying was determined to be less than 20 ppm by Karl Fisher titration using a Mettler-Toledo Coulometer. All the cells were assembled in an argon filled glove box. The specific capacitance of each electrode is calculated based on the formulae C_s (F g^{-1}) = 2(I x t)/(V x m), where I is the applied current (A), t is the

discharge time (s), V is operating voltage (V), and m is the CWMs mass in each electrode (g). Since, two electrode are employed in EDLCs, the energy density of the supercapacitor is calculated as $E = (C V^2/8)$ Wh kg^{-1}, and the power density is calculated as $P = (E/t)$ kW kg^{-1}.

3. Results and discussion

3.1. Structural & textural characterization of CWMs

Porous CWMs were synthesized from waste watermelon rind. The use of inexpensive and sustainable carbon sources renders this material economically viable for large scale applications such as electric vehicles and grid-scale energy storage systems. In addition, utilization of bio-waste as a carbon source reduces the environmental footprint of these storage systems [40,41]. Moreover, the lignin in bio-mass precursors majorly constitutes carbon, and nitro compounds which can facilitate in-situ doping of heteroatoms in carbon frameworks. The yield of the bulk carbon from dried watermelon rind was about ~40%. The TGA curves of watermelon rind powder in Figure S1 shows a steady weight loss between 200 °C to 600 °C, which are majorly due to the release of H_2O, CO_2 and CO. Moreover, the activation process was simple and a cost effective chemical activation (KOH) procedure was adopted at a relatively lower temperature (800 °C) in a short time. Unlike the commercial activated carbon produced by tedious physical activation processes (steam, CO_2) of coke at higher temperatures (> 1200 °C), the bio-mass carbon are synthesized more efficiently with lesser energy consumption. The higher yield of carbon, lower energy consumption and eco-friendliness of carbon precursor are favorable for large scale industrial production [21,22,24].

The morphology of the synthesized porous carbon was characterized using (SEM) and transmission electron microscope (TEM). The SEM images in Fig. 1a and 1b shows the presence of macropores, and the high resolution TEM images in Fig. 1c - 1d and Figure S2 indicates the presence of sub nanometer-sized pores. Nitrogen adsorption/desorption isotherms and pore size distributions of CWM were obtained to further understand the details of the pore architecture (Fig. 2a). The isotherm shows typical type IV characteristics with a steep initial region due to strong adsorption on micropores followed by a rounded knee, indicating the formation of monolayer [30,37]. The slopy region at higher relative pressures denotes multilayer adsorption on the mesopores. The presence of a hysteresis loop implies the existence of mesopores in the CWM. Also, NLDFT and BJH pore size distributions (Fig. 2a inset and 2b, respectively) show the distribution of micropores with the peak maximum at 1.3 nm and large concentration of mesopores between 2 and 4 nm. These results confirmed the presence of both mesoporous and microporous structures in CWM, which resulted in a high BET surface area of 2308 $m^2 g^{-1}$. Such a high surface area is comparable to the highest surface area ever reported for activated carbons derived from natural precursors [42,43]. The total pore volume and average pore size were measured to be 1.88 $cm^3 g^{-1}$, and 3.2 nm respectively. Based on the morphological and gas adsorption measurements, we confirmed the existence of hierarchical pore structures containing micro-, meso- and macropores in the CWM. The structural features of the CWM were studied using XRD analysis. The XRD pattern (Figure S3a) shows discernible broad peak between 20 and 30° which corresponds to (002) plane. Also, a broad peak at 43° is observed which is characteristic of (100) and (101) reflections and the peaks cannot be generally distinguished for such low crystalline compounds. This result indicates that there was no long-range ordering in the material and that the synthesized CWM was highly amorphous in nature [44]. The Raman spectrum of CWM (Figure S3b) showed two characteristic bands at 1602 and 1356 cm^{-1}, corresponding to G- and D-bands, respectively [45]. The G band arose from the sp^2-hybridized graphitic carbons, and the D band was attributed to the sp^3 distortion induced by the local

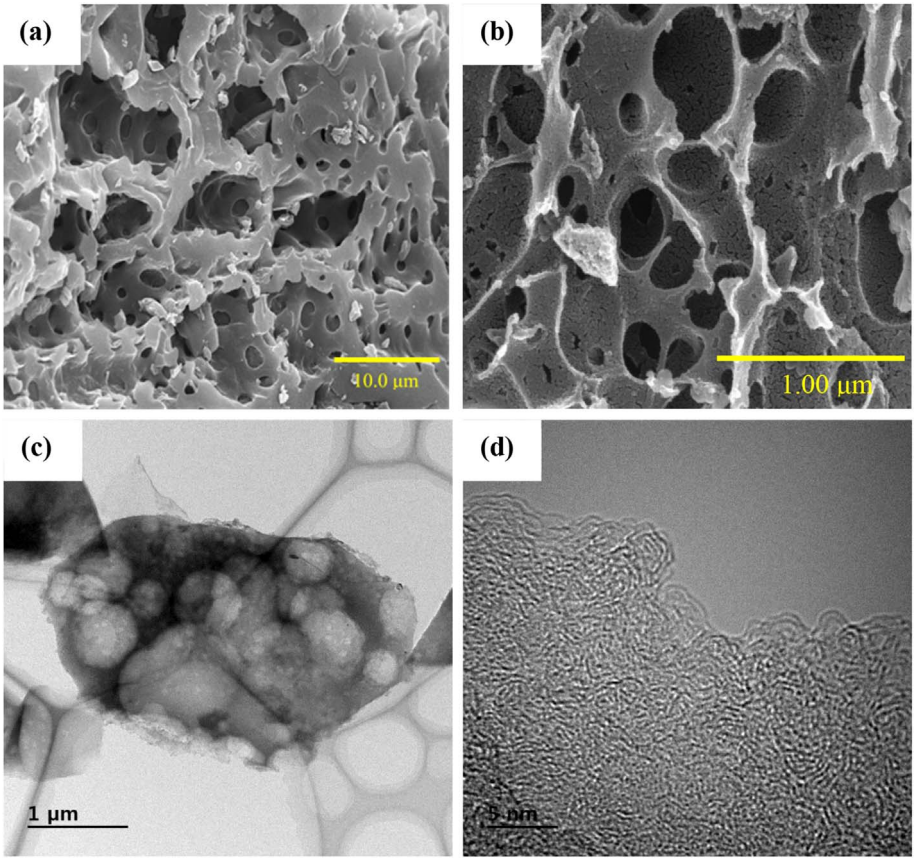

Fig. 1. (a) & (b) SEM images of CWMs, and (c) & (d) TEM images of CWMs.

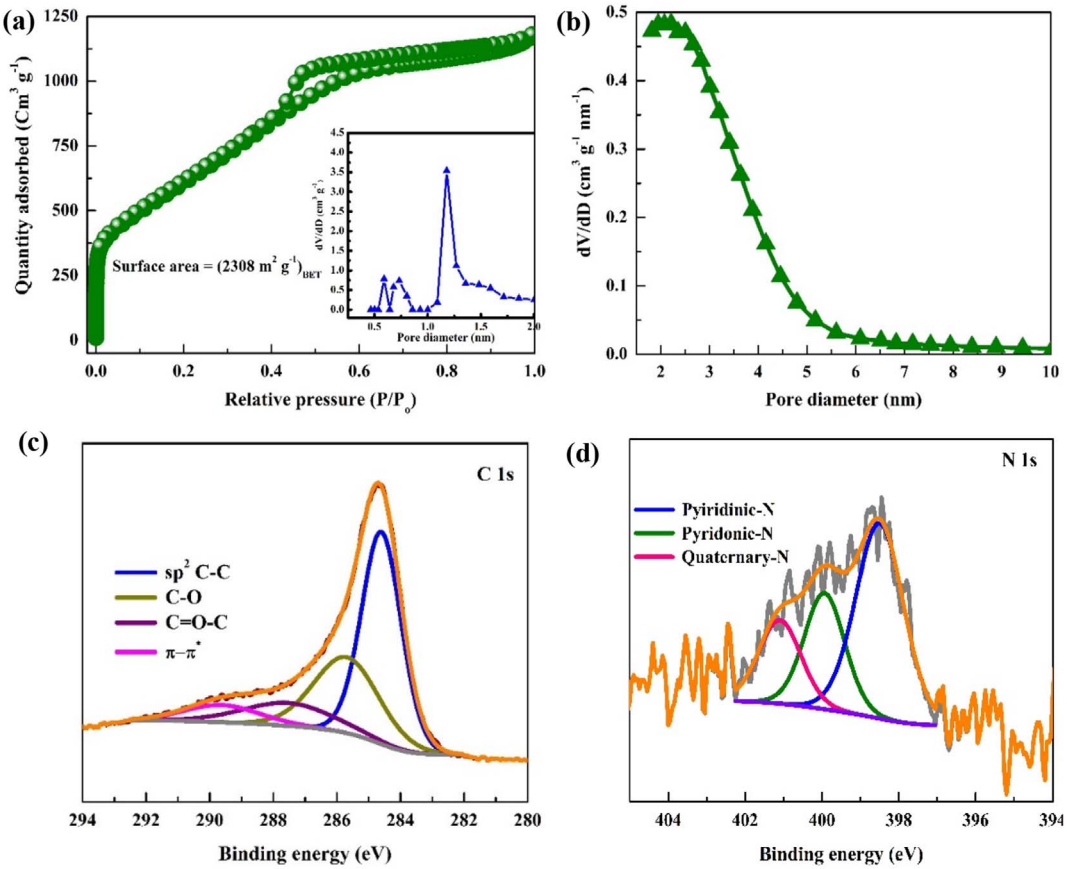

Fig. 2. (a) Nitrogen adsorption/desorption isotherm of CWM; Inset: NLDFT pore size distribution, and (b) BJH pore size distribution, (c) high-resolution C 1s XPS spectra of CWM, and (d) high-resolution N 1s XPS spectra.

plane derivatization. The G-band position of graphitic carbon is generally observed at around 1570 cm^{-1}. However, the G-band was blue-shifted to 1602 cm^{-1}, indicating significant amorphization of carbon. The presence of amorphous carbon resulted in broadening of the G-band as well. These results show that the as-prepared CWM was highly amorphous in nature, which further confirmed the XRD results [45,46]. The electrical conductivity of the CWM was calculated to be ~2.8 S cm^{-1}, highly comparable to the commercial activated carbons.

3.2. Chemical composition of CWMs

Table S1 shows the bulk and surface composition of activated CWMs deduced by elemental analysis and XPS respectively, listing the weight percentage of major constituents (C, O, N, H). The significant amount nitrogen hetero atoms greatly contribute towards the good conductivity of CWMs. The surface chemical composition of CWM was characterized using XPS, and the results are given in Figure S3c. The XPS survey spectrum shows the presence of carbon and oxygen in CWM along with a significant amount of nitrogen heteroatoms (2.21 wt %). Based on the XPS spectrum, the content of Si impurities is ~0.92 wt %. Other potential metal impurities that may be present in bio-mass precursors were below the XPS detection limit, which were removed during post acid washing (HCl) step. The presence of heteroatoms can enhance the wettability of the electrode surface and reduce the surface resistance by providing a large number of active adsorption sites. To further understand the nature of functional groups present on the CWM surface, a high-resolution C 1s spectrum was deconvoluted into four peaks as shown in Fig. 2c. The peaks centered at 284.6 and 285.9 eV correspond to sp^2-hybridized carbon and C-O groups, respectively. The peaks observed at 287.6, and 290.3 eV were attributed to carbonyl groups, and π-π* interactions, respectively. The deconvoluted N1s spectrum in Fig. 2d exhibits three major peaks corresponding to pyridinic-N (398.5 eV), pyrrolic-N (400.1) and quaternary-N (401.1 eV) [45].

3.3. Supercapacitor performance

The capacitive behavior of CWM was evaluated at various operating voltages and current densities by assembling two-electrode symmetric cells. Also, to verify the broad applicability of CWM-based supercapacitors, the electrochemical studies were carried out at room temperature (25 °C) and at high temperature (60 °C). An ionic liquid electrolyte, EMImTFSI was chosen as an electrolyte to extend the operating voltage and to achieve a high energy density.

The capacitive behavior of CWM was initially investigated by cyclic voltammetry at different scan rates in the potential window of 0–4 V at both room temperature (25 °C) and high temperature (60 °C). As shown in Fig. 3a and Figure S4, the cyclic voltammograms (CVs) exhibited a rectangular shape up to 4 V, confirming that the capacitance obtained was mainly due to electric double layer formation [47]. Supercapacitors assembled with CWM electrodes retained their rectangular shaped profile even at a high scan rate of 200 mV s^{-1}. The galvanostatic charge-discharge behavior of supercapacitor was investigated at different current densities in the voltage range of 0–4 V. The charge-discharge curves obtained at 25 and 60 °C are shown in Fig. 3b and c, respectively. The obtained curves exhibited a symmetrical triangular shaped profile at all the current rates irrespective of the operating temperature and these data are in good agreement with the CV results. [48] [49].

At a current density of 1 A g^{-1}, the supercapacitor assembled with CWM electrodes delivered a remarkable specific capacitance of 313 F g^{-1} and 320 F g^{-1} at 25 °C, and 60 °C respectively. For comparison, commercial activated carbon (CAC) was also tested for the

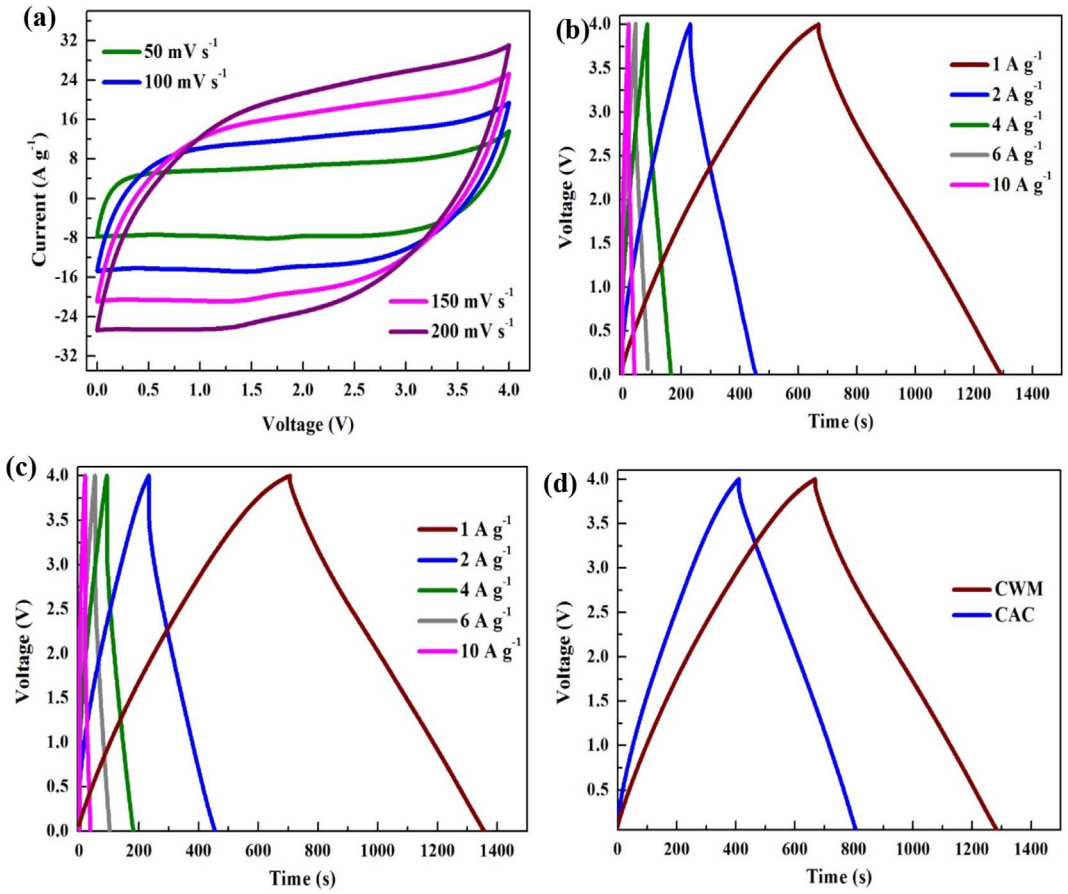

Fig. 3. (a) Cyclic voltammograms of CWM at 60 °C, (b) CD curves of CWM at 25 °C, (c) CD curves of CWM at 60 °C, and (d) Comparison of CD curves of CWM and commercial activated carbon at 1 A g^{-1} (25 °C).

supercapacitor application using the same testing conditions. Supercapacitors assembled with CAC showed shorter discharge time and a low capacitance (~202 F g^{-1} at 1 A g^{-1}) than CWMs (Fig. 3d). This poor performance of CAC is mainly due to its low surface area along with highly micrporous nature, which does not provide large number of active sites for large sized ions from the ionic liquids to get adsorbed (Characterization of CAC is shown in supporting information) [50]. However, CWMs being an ultra-high surface area carbon with a combination of micro- and meso pores, provide a large number of active pores for adsorption process easily. The achieved high capacitance was mainly attributed to the extended operating voltage using an ionic liquid electrolyte as well as the complete utilization of micropores present in CWM that were easily accessed through the mesopore channels [51–53]. The specific capacitance value of CWMs obtained at this current density even surpassed the performance of supercapacitors based on conventional porous carbon, where the reported specific capacitances were around 200 to 250 F g^{-1}.

It should be noted that such a high capacitance with a wide operating voltage (4 V) could increase the energy density of supercapacitor by several orders. The capacitance decreased with increasing current density, which was mainly ascribed to the resistance developed over the movement of electrolyte ions towards the pore wall. The supercapacitor tested at elevated temperature delivered higher specific capacitances at all current densities than the cell tested at room temperature (Fig. 4a). This result can be attributed to the reduced viscosity of ionic liquid electrolyte at elevated temperature, which resulted in enhanced ionic conductivity. This can be visualized from impedance spectra in Fig. 4b of CWM supercapacitors, where solution resistance and charge transfer resistance were greatly reduced at elevated temperature [54,55]. Despite using an ionic liquid electrolyte, the supercapacitor with CWM electrodes still delivered a high specific capacitance of 45 (25° C) and 65 (60° C) F g^{-1} at 20 A g^{-1}. Such a good rate performance was attributed to high surface area and narrow pore size distribution, where micropores and mesopores smaller than 4 nm were present. Here, meso and micropores synergistically contributed towards double layer formation by efficiently enhancing the electrolyte diffusion and ionic adsorption. The mesoporous hierarchal architecture greatly reduces the ion transport time by providing short transport distance to the inner most pores. The larger mesopores synergistically function as electrolyte reservoir and supply ions to deeper pores through a short ion diffusion path [56].

3.4. Energy – power behavior of supercapacitor

To further substantiate the superiority of our system, Ragone plot was constructed and compared with other supercapacitor devices and commercial energy storage systems. The energy and power densities of supercapacitors assembled with CWM electrodes are presented in a Ragone plot and compared with other supercapacitor systems (Fig. 4c). Table 1 compares the performances of the current system with other capacitors based on ionic liquid electrolytes. Based on the active mass in both electrodes, the CWM delivered an exceptional energy density of 174 Wh kg^{-1} at 25 °C, the highest ever energy density achieved than state-of-the-art capacitors based on activated carbon, graphene, carbon nanotubes, porous carbon from various precursors and modified carbon structures. This high energy density was possible only because of the wide operating voltage and complete utilization of pore walls for double layer formation. The CWM-based high energy supercapacitor exhibited superior performance by retaining an energy density of 27.5 Wh kg^{-1} at a high power density of 20 kW kg^{-1} at 25 °C. At 60 °C, the

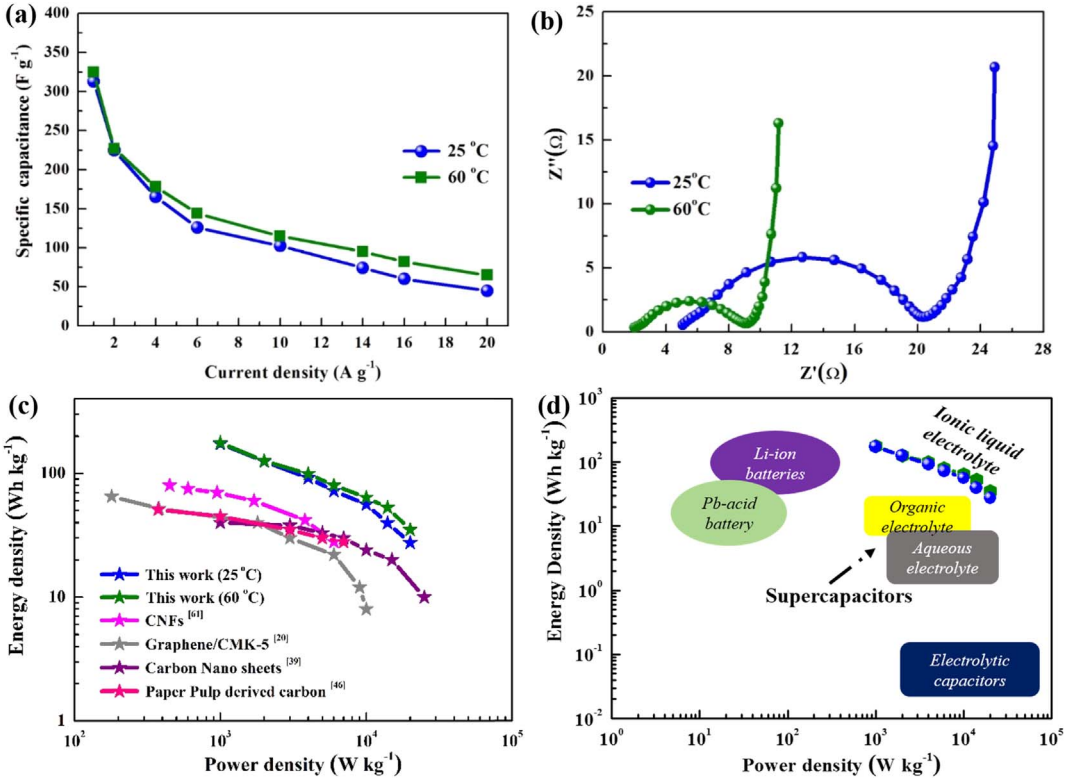

Fig. 4. (a) Rate performance of CWM supercapacitor at 25 and 60 °C, (b) Nyquist plots of CWM supercapacitors, (c) & (d) Ragone plots displaying energy – power performance.

cell delivered a much higher energy density of 178 Wh kg^{-1}, and a maximum power density of 20 kW kg^{-1} was achieved at an energy density of 35 Wh kg^{-1}.

Also, Fig. 4d compares the performance of current 4 V supercapacitor with other energy storage systems. It can be clearly visualized that the current system delivered specific energy and specific power several orders higher than conventional aqueous and organic supercapacitors. The obtained energy densities were not only superior to the values of conventional capacitors, but were also superior to recent hybrid capacitor systems and were on par with modern rechargeable batteries. As seen from Table 1, the assembled supercapacitor outperformed various porous carbon and graphene based materials by several orders.

3.5. Cyclic stability of supercapacitor

Apart from high energy and power densities, a stable cyclic performance is indispensable for a superior energy storage device. However, most supercapacitors employing ionic liquids did not study this feature or reported cyclic stability less than 1000 cycles. In order to evaluate the cycling stability, the cells were tested under harsh charge-discharge conditions in the voltage range of 0–4 V at a current density

Table 1
Comparison of specific capacitance, energy density, power density and stability of various capacitor systems with the current work.

Stability						
Material	Electrolyte	Specific capacitance (F g-1)	Energy density (Wh kg-1)	Power density (kW kg^{-1})	% retention	Cycles
CWM (This work) (25 °C)	EMIM TFSI (0–4 V)	313 (l A g^{-1})	174	20	85 (10 A g^{-1})	20000
(60 °C)	EMIM TFSI (0–4 V)	325 (1 A g^{-1})	177	20	45 (10 A g^{-1})	10000
Carbon nanofibers [61]		180 (0.5 A g^{-1})	80	10	83 (5 A g^{-1})	5000
2D carbon/graphene [30]	1.0 M $TEABF_4$/AN (0–2.7 V)	276 (1 A g^{-1})	70	27	97 (30 A g^{-1})	8000
3D ordered mesoporous carbon [58]	EMIM TFSI (0–3.5 V)	178 (0.5 A g^{-1})	64		90 (5 A g^{-1})	1000
Graphene/CMK-5 [20]	EMIM BF_4 (0–3.5 V)	145 (0.2 A g^{-1})	61	90 (2 A g^{-1})		2000
Hemp derived carbon nanosheets [39]	BMPY TFSI (0–3 V)	160 (0.5 A g^{-1})	40	20	96 (10 A g^{-1})	10000
Poiypyrrole derived carbon [37]	EMIM BF_4 (0–2.3 V)	120			95–98 (10 A g^{-1})	10000
Hard templated carbon [31]	EMIM TFSI (0–3.5 V)	237 (0.1 A g^{-1})	101		85 (1 A g^{-1})	1100
High surface area bimodal carbon [33]	EMIM TFSI in AN (0–3 V)	160 (1 A g^{-1})	60	42	85 (5 A g^{-1})	10000
Curved graphene [18]	EMIM BF_4 (0–4 V)	154 (1 A g^{-1})	136	10	Not studied	
Poly IL modified graphene [59]	EMIM-NTf, (0–3.5 V)	185 (1 A g^{-1})	74	20	Not studied	
Glucose derived carbon [64]	EMIM BF_4 (0–3.2 V)	158 (1 mV s^{-1})	45	10	Not studied	
Activated carbon [63]	$BMPyNTf_2$ (0–3V)	180 (5 mV s^{-1})	77		Not studied	
Carbide derived carbon [15]	EMIM BF_4 (0–3 V)	160 (3 A g^{-1})	68		Not studied	
Activated graphene [23]	$TEABF_4$ in AN (0–2.7 V)	I8O (2A g^{-1})	76		Not studied	
Carbon/PIM [29]	EMIM BF_4 (0–4 V)	120 (10 mV s^{-1})	60	1.7	Not studied	

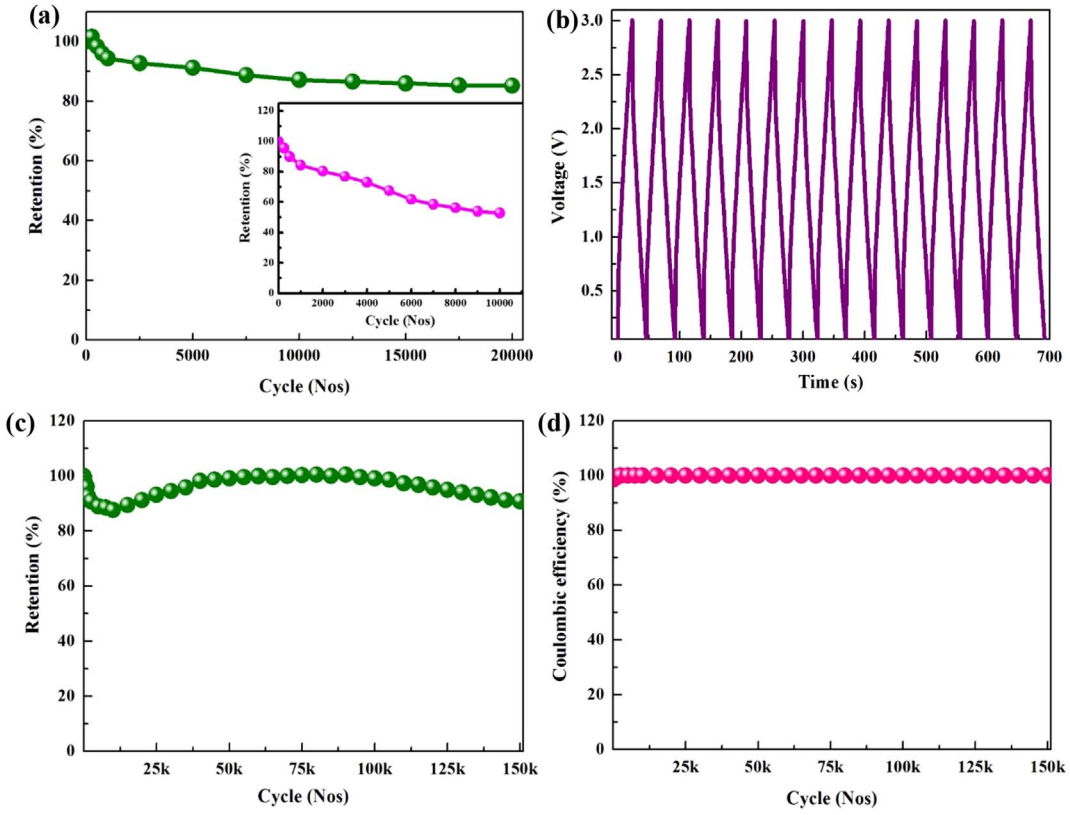

Fig. 5. (a) Cyclic stability of CWM at 25 °C between 0 and 4 V, Inset: cyclic stability at 60 °C between 0 and 4 V, (b) continuous CD profile between 0 and 3 V at 60 °C, (c) cyclic stability of CWM between 0 and 3 V at 60 °C, and (d) coulombic efficiency between 0 and 3 V at 60 °C.

of 10 A g^{-1} (Fig. 5a). The supercapacitor exhibited stable cycling performance up to 20,000 cycles at 25 °C. This is the most stable high energy capacitor ever reported using an ionic liquid electrolyte, and it surpasses the cycling stability reported in previous literature based on curved graphene, activated carbon, activated graphene, hard templated carbon, carbon nanovesicles, 3-D ordered mesoporous carbon and carbon nanofibers [18,20,23,29–31,37,58–64]. However, the cell tested at 60 °C retained only ~48% of its initial capacitance after 10,000 cycles (Inset: Fig. 5a). This result was ascribed to the unstable nature of ionic liquid electrolyte with carbon electrodes when operated at elevated temperature over a high voltage range.

To achieve stable cycling performance at 60 °C, the operating voltage was adjusted between 0 and 3.5 V, which is still a high voltage for supercapacitors at elevated temperatures. A remarkable change in stability is noted after reducing the operational voltage at high temperature and ~74% retention is noted after 10,000 cycles (Figure S6). The operational potential window was further reduced to 0-3 V expecting a better stability at high temperature. The charge-discharge curves between 0 and 3 V (Fig. 5b) showed similar symmetrical triangular-shaped profiles, and the CVs (Figure S7) exhibited rectangular shapes, indicating its capacitive behavior. An interesting feature in the cycling behavior of the ionic liquid based capacitor assembled with CWM was that the specific capacitance decreased during initial cycling and then increased to achieve a maximum specific capacitance (Fig. 5c). This is in contrast to the cycling performance of capacitors in a high potential window (4 V), where the specific capacitance declined steadily throughout cycling. This indicates that the electrolyte decomposed at higher potentials (especially under high temperature operation), and the decomposition product generally includes sulphides, sulphates and fluorocarbonates. Additionally, with EMImTFSI ionic liquid electrolyte the cations are not electrochemically stable at high temperature due to the presence of acidic proton [57,62]. The continuous electrolyte decomposition decreases the ionic conductivity of the electrolyte and there reducing the continuous free ion movement with cycling.

Electrolyte was stable in the voltage range of 0–3 V at 60 °C, and the pores were activated upon cycling, resulting in an increase in specific capacitance. The increase in capacitance with cycling is a general phenomenon observed in supercapacitors employing porous carbonaceous electrodes and highly viscous ionic liquid electrolyte [37]. With continuous cycling, the unutilized active materials during the initial cycles participate in the electrochemical reaction and thereby increasing the capacitance. This is majorly because of the delayed infiltration of highly viscous ionic liquid into the deeper pores, leading to availability of more active pores with cycling for ion adsorption process [62]. The cell retained 90% of its initial capacitance after 150,000 cycles at 10 A g^{-1} and 60 °C with ~100% coulombic efficiency throughout cycling (Fig. 5d). Even after cycling, the shape profile of charge-discharge curves were well maintained in a similar fashion and only a negligible change in discharge time was noted (Figure S7). Such a highly stable performance by any high energy capacitor system has never been reported previously. The advantage of good cycling stability at this condition is that the device can efficiently maintain its energy density for longer cycles. The good cycling stability of this cell was mainly ascribed to the stable nature of ionic liquid electrolyte in this voltage range at high temperature. Moreover, the presence of nitrogen functional groups on the pore walls improved the wettability of the electrolyte on pore walls. The surface wettability nature of CWMs and CACs confirmed by contact measurements with ionic liquid electrolyte (Figure S8) where CWMs shows an improved electrolyte wettability than CACs. Additionally, the impedance spectra of CWM and CAC in Figure S9 confirms a lower surface resistance of CWMs than CACs. This increased the amount of electrolyte stored inside the pores and thereby provided easy access of ions to the pore wall to establish a double layer. In addition, the mechanical strength of the CWM carbon frameworks was high enough to withstand the harsh testing conditions and prevent any structural damage.

The superior performance of the high energy supercapacitor in this work was mainly attributed to the following factors. (i) The CMW had a large accessible surface area and hierarchical pores with large pore volume that can easily fit large sized ions from the highly viscous ionic liquid even at high current rates, (ii) CMW had a favorable pore size distribution with a combination of large micropores (> 1 nm) and small mesopores (< 4 nm), which improved the kinetics of ionic movement and enabled maximum pore utilization even at high currents, (iii) The presence of nitrogen functional groups on the surface improved the wettability of the carbon surface and thereby promoted ion access to the pore wall, (iv) The high compatibility of the ionic liquid with the CWM over a wide operating voltage and elevated temperature helped to maintain the pore structure without any deterioration, and thereby maintained stability even under harsh conditions.

4. Conclusion

A hierarchically porous carbon with a large surface area and narrow pore size distribution was synthesized from a sustainable and renewable bio-waste. Our results demonstrated its potential application in next-generation high energy density, fast working green storage devices. The supercapacitors assembled with CWM electrodes exhibited a remarkable performance even with a highly viscous ionic liquid electrolyte at room temperature. A maximum energy density of 174 Wh kg^{-1} and a specific power of 20 kW kg^{-1} was achieved with diffusion limited ionic liquid electrolyte utilizing a tailored porous carbon. Additionally, the supercapacitor showed an excellent cycling stability at 60 °C with 90% retention even after 150,000 cycles. The favorable architecture of CWM towards energy storage for high energy density devices, made them to outperform the devices made with conventioanal porous carbon. This simple strategy that utilizes bio-wastes for next-generation energy storage devices could provide a sustainable long-term solution to achieve high energy efficiency and address increasing environmental concerns.

Acknowledgements

This work was supported by the National Research Foundation of Korea (NRF) grant funded by the Korea government (Ministry of Science, ICT and Future Planning) (No. 2016R1A4A1012224).

Appendix A. Supplementary data

Supplementary data related to this article can be found at http://dx.doi.org/10.1016/j.jpowsour.2018.02.037.

References

[1] S. Chu, A. Majumdar, Nature 488 (2012) 294–303.
[2] K. Kang, Y.S. Meng, J. Bréger, C.P. Grey, G. Ceder, Science 311 (2006) 977–980.
[3] J.R. Miller, P. Simon, Science 321 (2008) 651–652.
[4] M. Armand, J.M. Tarascon, Nature 451 (2008) 652–657.
[5] J.M. Tarascon, M. Armand, Nature 414 (2001) 359–367.
[6] H. Pan, Y.-S. Hu, L. Chen, Energy Environ. Sci. 6 (2013) 2338–2360.
[7] R. Thangavel, A. Samuthira Pandian, H.V. Ramasamy, Y.-S. Lee, ACS Appl. Mater. Interfaces 9 (2017) 40187–40196.
[8] R. Thangavel, K. Kaliyappan, D.-U. Kim, X. Sun, Y.-S. Lee, Chem. Mater. 29 (2017) 7122–7130.
[9] R. Thangavel, B. Moorthy, D.K. Kim, Y.-S. Lee, Adv. Energy Mater (2017) 1602654.
[10] R. Thangavel, K. Kaliyappan, K. Kang, X. Sun, Y.-S. Lee, Adv. Energy Mater. 6 (2016) 1502199.
[11] J.R. Rani, R. Thangavel, S.-I. Oh, J.M. Woo, N. Chandra Das, S.-Y. Kim, Y.-S. Lee, J.-H. Jang, ACS Appl. Mater. Interfaces 9 (2017) 22398–22407.
[12] L. Yu, L. Zhang, H.B. Wu, X.W. Lou, Angew. Chem. Int. Ed. 53 (2014) 3711–3714.
[13] M. Inagaki, H. Konno, O. Tanaike, J. Power Sources 195 (2010) 7880–7903.
[14] J.R. Miller, J. Power Sources 326 (2016) 726–735.
[15] A.G. Kannan, A. Samuthirapandian, D.-W. Kim, J. Power Sources 337 (2017) 65–72.
[16] H. Ji, X. Zhao, Z. Qiao, J. Jung, Y. Zhu, Y. Lu, L.L. Zhang, A.H. MacDonald, R.S. Ruoff, Nat. Commun. 5 (2014) 3317.
[17] H.V. Ramasamy, K. Kaliyappan, R. Thangavel, V. Aravindan, K. Kang, D.U. Kim, Y. Park, X. Sun, Y.-S. Lee, J. Mater. Chem. A 5 (2017) 8408–8415.
[18] C. Liu, Z. Yu, D. Neff, A. Zhamu, B.Z. Jang, Nano Lett. 10 (2010) 4863–4868.
[19] K.L. Van Aken, M. Beidaghi, Y. Gogotsi, Angew. Chem. Int. Ed. 54 (2015) 4806–4809.
[20] Z. Lei, Z. Liu, H. Wang, X. Sun, L. Lu, X.S. Zhao, J. Mater. Chem. 1 (2013) 2313–2321.
[21] A. Balducci, J. Power Sources 326 (2016) 534–540.
[22] R. Thangavel, K. Kaliyappan, H. Ramasamy, X. Sun, Y.-S. Lee, ChemSusChem 10 (2017) 2805–2815 10.
[23] L.L. Zhang, X. Zhao, M.D. Stoller, Y. Zhu, H. Ji, S. Murali, Y. Wu, S. Perales, B. Clevenger, R.S. Ruoff, Nano Lett. 12 (2012) 1806–1812.
[24] H. Yang, S. Kannappan, A.S. Pandian, J.-H. Jang, Y.S. Lee, W. Lu, J. Power Sources 284 (2015) 146–153.
[25] Y. Wen, T.E. Rufford, D. Hulicova-Jurcakova, L. Wang, ChemSusChem 9 (2016) 513–520.
[26] H. Wu, Y. Zhang, L. Cheng, L. Zheng, Y. Li, W. Yuan, X. Yuan, Energy Storage Mater. 5 (2016) 8–32.
[27] L. Eliad, G. Salitra, A. Soffer, D. Aurbach, J. Phys. Chem. B 105 (2001) 6880–6887.
[28] E. Frackowiak, F. Béguin, Carbon 39 (2001) 937–950.
[29] Y. Ren, J. Zhang, Q. Xu, Z. Chen, D. Yang, B. Wang, Z. Jiang, RSC Adv. 4 (2014) 23412–23419.
[30] D.Y. Chung, K.J. Lee, S.-H. Yu, M. Kim, S.Y. Lee, O.-H. Kim, H.-J. Park, Y.-E. Sung, Adv. Energy Mater. 5 (2015) 1401309.
[31] B.E. Wilson, S. He, K. Buffington, S. Rudisill, W.H. Smyrl, A. Stein, J. Power Sources 298 (2015) 193–202.
[32] J. Ajuria, E. Redondo, M. Arnaiz, R. Mysyk, T. Rojo, E. Goikolea, J. Power Sources 359 (2017) 17–26.
[33] M. Sevilla, A.B. Fuertes, Carbon 47 (2009) 2281–2289.
[34] W. Yang, M. Ni, X. Ren, Y. Tian, N. Li, Y. Su, X. Zhang, Curr. Opin. Colloid Interface sci. 20 (2015) 416–428.
[35] Z.-Q. Hao, J.-P. Cao, Y. Wu, X.-Y. Zhao, Q.-Q. Zhuang, X.-Y. Wang, X.-Y. Wei, J. Power Sources 361 (2017) 249–258.
[36] Q. Liang, L. Ye, Z.-H. Huang, Q. Xu, Y. Bai, F. Kang, Q.-H. Yang, Nanoscale 6 (2014) 13831–13837.
[37] S. Zhao, T. Yan, Z. Wang, J. Zhang, L. Shi, D. Zhang, RSC Adv. 7 (2017) 4297–4305.
[38] X.-L. Wu, T. Wen, H.-L. Guo, S. Yang, X. Wang, A.-W. Xu, ACS Nano 7 (2013) 3589–3597.
[39] H. Wang, Z. Xu, A. Kohandehghan, Z. Li, K. Cui, X. Tan, T.J. Stephenson, C.K. King'ondu, C.M.B. Holt, B.C. Olsen, J.K. Tak, D. Harfield, A.O. Anyia, D. Mitlin, ACS Nano 7 (2013) 5131–5141.
[40] W. Huang, H. Zhang, Y. Huang, W. Wang, S. Wei, Carbon 49 (3) (2011) 838–843.
[41] L. Wei, G. Yushin, Carbon 49 (14) (2011) 4830–4838.
[42] Y. Zhai, Y. Dou, D. Zhao, P.F. Fulvio, R.T. Mayes, S. Dai, Adv. Mater 23 (2011) 4828–4850.
[43] X.-L. Su, M.-Y. Cheng, L. Fu, J.-H. Yang, X.-C. Zheng, X.-X. Guan, J. Power Sources 362 (2017) 27–38.
[44] H. Jiang, P.S. Lee, C. Li, Energy Environ. Sci. 6 (2013) 41–53.
[45] L. Lafi, D. Cossement, R. Chahine, Carbon 43 (2005) 1347–1357.
[46] R. Karthick, M. Brindha, M. Selvaraj, S. Ramu, J. Colloid Interface Sci. 406 (2013) 69–74.
[47] M. Nazarian-Samani, S. Haghighat-Shishavan, M. Nazarian-Samani, M.-S. Kim, B.-W. Cho, S.-H. Oh, S.F. Kashani-Bozorg, K.-B. Kim, J. Power Sources 372 (2017) 286–296.
[48] N. Guo, M. Li, X. Sun, F. Wang, R. Yang, Green Chem. 19 (2017) 2595–2602.
[49] L. Zhou, H. Cao, S. Zhu, L. Hou, C. Yuan, Green Chem. 17 (2015) 2373–2382.
[50] J. Ding, H. Wang, Z. Li, K. Cui, D. Karpuzov, X. Tan, A. Kohandehghan, D. Mitlin, Energy Environ. Sci. 8 (2015) 941–955.
[51] D. Hulicova-Jurcakova, M. Kodama, S. Shiraishi, H. Hatori, Z.H. Zhu, G.Q. Lu, Adv. Funct. Mater. 19 (2009) 1800–1809.
[52] Y. Zhang, S. Liu, X. Zheng, X. Wang, Y. Xu, H. Tang, F. Kang, Q.-H. Yang, J. Luo, Adv. Funct. Mater. 27 (2017) 1604687.
[53] D. Lozano-Castelló, D. Cazorla-Amorós, A. Linares-Solano, S. Shiraishi, H. Kurihara, A. Oya, Carbon 41 (2003) 1765–1775.
[54] M.D. Stoller, S. Murali, N. Quarles, Y. Zhu, J.R. Potts, X. Zhu, H.-W. Ha, R.S. Ruoff, Phys. Chem. Chem. Phys. 14 (2012) 3388–3391.
[55] L.L. Zhang, X. Zhao, M.D. Stoller, Y. Zhu, H. Ji, S. Murali, Y. Wu, S. Perales, B. Clevenger, R.S. Ruoff, Nano Lett. 12 (2012) 1806–1812.
[56] Y. Chen, X. Zhang, H. Zhang, X. Sun, D. Zhang, Y. Ma, RSC Adv. 2 (2012) 7747–7753.
[57] S.P. Ong, O. Andreussi, Y. Wu, N. Marzari, G. Ceder, Chem. Mater. 23 (2011) 2979–2986.
[58] A. Vu, X. Li, J. Phillips, A. Han, W.H. Smyrl, P. Bühlmann, A. Stein, Chem. Mater. 25 (2013) 4137–4148.
[59] T.Y. Kim, H.W. Lee, M. Stoller, D.R. Dreyer, C.W. Bielawski, R.S. Ruoff, K.S. Suh, ACS Nano 5 (2011) 436–442.
[60] M. Ghaffari, Y. Zhou, H. Xu, M. Lin, T.Y. Kim, R.S. Ruoff, Q.M. Zhang, Adv. Mater. 25 (2013) 4879–4885.
[61] C. Tran, D. Lawrence, F.W. Richey, C. Dillard, Y.A. Elabd, V. Kalra, Chem. Commun 51 (2015) 13760–13763.
[62] P. Schmitz, R. Jakelski, M. Pyschik, K. Jalkanen, S. Nowak, M. Winter, P. Bieker, ChemSusChem 10 (2017) 876–883.
[63] A. Lewandowski, M. Galiński, J. Phys. Chem. Solids 65 (2004) 281–286.
[64] T. Tooming, T. Thomberg, H. Kurig, A. Jänes, E. Lust, J. Power Sources 280 (2015) 667–677.